

# A Comprehensive Scenario of the Crystal Growth of $\gamma$ -Bi<sub>2</sub>MoO<sub>6</sub> Catalyst during Hydrothermal Synthesis

Chanapa Kongmark,<sup>†,‡</sup> Rachel Coulter,<sup>†</sup> Sylvain Cristol,<sup>†</sup> Annick Rubbens,<sup>†</sup> Caroline Pirovano,<sup>†</sup> Axel Löfberg,<sup>†</sup> Gopinathan Sankar,<sup>§</sup> Wouter van Beek,<sup>||,⊥</sup> Elisabeth Bordes-Richard,<sup>†</sup> and Rose-Noëlle Vannier<sup>\*,†</sup>

<sup>†</sup>Unité de Catalyse et de Chimie du Solide, UMR CNRS 8181, Université Lille 1, ENSCL, BP 90108, 59652 Villeneuve d'Ascq Cedex, France

<sup>‡</sup>Synchrotron Light Research Institute, 111 University Avenue, Muang, P.O. Box 93, 30000 Nakhon Ratchasim, Thailand

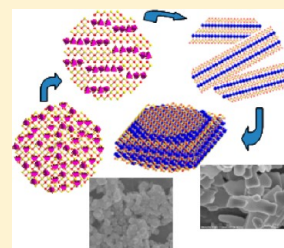
<sup>§</sup>Department of Chemistry, University College London, 20 Gordon Street, WC1H 0AJ London, United Kingdom

<sup>||</sup>SNBL at ESRF, 6 rue Jules Horowitz, 38043 Grenoble, France

<sup>⊥</sup>Dipartimento di Scienze e Tecnologie Avanzate, Università del Piemonte Orientale "A. Avogadro", Via V. Bellini 25/G, 15100 Alessandria, Italy

## Supporting Information

**ABSTRACT:** In a previous study, we confirmed by in situ combined high-resolution powder diffraction/X-ray absorption spectroscopy and Raman scattering experiments that the crystal formation of the well-known  $\gamma$ -Bi<sub>2</sub>MoO<sub>6</sub> catalyst occurred in two steps through the formation of an intermediate fluorite structure (Kongmark, C. et al. *Chem. Commun.* **2009**, 4850–4852; *Catal. Today* **2010**, 157, 257–262). Here, for the first time, by combining these results with complementary ex situ studies (HTXRD, SEM/EDX, Raman scattering), it was possible to elucidate the nature of the intermediate phase and to propose a complete scenario of the growth of  $\gamma$ -Bi<sub>2</sub>MoO<sub>6</sub> crystals. In addition, we performed a kinetic analysis from the three different in situ characterization techniques and confirmed a 2D-diffusion limited growth process.



## 1. INTRODUCTION

Bismuth-based mixed oxides with a layered structure, known as Aurivillius phases,<sup>1</sup> have early drawn significant research interest. For applications in heterogeneous catalysis, bismuth molybdate was shown to be active and selective in the oxidative dehydrogenation of butene and in the (amm)oxidation of propylene to acrolein and acrylonitrile.<sup>2–5</sup> Since the 1970s, multicomponent molybdate catalysts have been industrially used in the latter reactions. The discovery of new Aurivillius oxides continues to bring forward materials with key properties and applications in materials science, such as fast ion conductors like BIMEVOX,<sup>6–8</sup> including their application in catalytic dense membrane reactors<sup>9,10</sup> and ferroelectric and magnetic materials (bismuth titanate and bismuth ferrite).<sup>1,11–13</sup> The bidimensional structure built upon perovskite-like units alternated with [Bi<sub>2</sub>O<sub>2</sub>]<sup>2+</sup> bismuth–oxygen sheets is responsible for their exceptional properties.<sup>1,14</sup> Such compounds are usually prepared by a solid-state route that requires a high annealing temperature, and usually delivers powders with a low specific surface area. For catalytic applications, other methods (e.g., coprecipitation,<sup>15</sup> sol–gel and spray drying,<sup>16–18</sup> hydrothermal synthesis<sup>19–21</sup>) were used to prepare bismuth molybdates with the aim of improving their surface area, crystallinity, and morphology, all characteristics that exert significant influence on their catalytic properties. Among these methods, the hydrothermal synthesis is appropriate as highly pure and crystalline particles, charac-

terized by a narrow size distribution and low aggregation, are obtained.<sup>22,23</sup> The crystallization of  $\gamma$ -Bi<sub>2</sub>MoO<sub>6</sub> in hydrothermal conditions was studied by Beale et al., who performed in situ energy-dispersive X-ray diffraction (EDXRD) and combined XRD/XAS techniques at low temperature.<sup>20,22,23</sup>

Aiming at optimizing the conditions of production of the  $\gamma$ -Bi<sub>2</sub>MoO<sub>6</sub> catalyst by controlling its crystal growth, we carried out in situ experiments at the European Synchrotron Radiation Facility. For the first time, X-ray diffraction, XANES, and Raman spectroscopy were combined to examine in situ the hydrothermal synthesis.<sup>24</sup> We confirmed that the crystal formation occurred in two steps through the formation of an intermediate fluorite structure, but the nature and structure of the intermediary compound close to Bi<sub>2</sub>O<sub>3</sub>, which was not mentioned in former ex situ studies,<sup>21</sup> could not be precisely determined. Some complementary experiments were carried out on particles obtained at 180 °C while varying the synthesis time.<sup>25</sup> The formation of spherical particles was evidenced after 30 min, and platelet-like particles of  $\gamma$ -Bi<sub>2</sub>MoO<sub>6</sub> were occurring for a longer duration.

In the present paper, the kinetic analysis using data from three different characterization techniques was compared for the first time, XAS and Raman spectroscopy probing the

**Received:** July 27, 2012

**Revised:** October 31, 2012

**Published:** November 2, 2012

transformation of molybdenum species, and HRPD monitoring the transformations of the crystals. Complementary *ex situ* experiments by high-temperature X-ray diffraction/scanning electron microscopy/EDX and Raman scattering made it possible to elucidate the nature of the intermediate phase, and to propose a scenario of the mechanism of  $\gamma$ - $\text{Bi}_2\text{MoO}_6$  formation.

## 2. EXPERIMENTAL SECTION

**Materials.** Bismuth oxide  $\text{Bi}_2\text{O}_3$  (Riedel-de-Haën, 99.5%) preheated at 600 °C for decarbonation, ammonium heptamolybdate tetrahydrate  $(\text{NH}_4)_6\text{Mo}_7\text{O}_{24}\cdot 4\text{H}_2\text{O}$  (Janssen Chimica, 99%), 65% (w/w) nitric acid  $\text{HNO}_3$  (VWR Prolabo Normapur), and 28% (w/w)  $\text{NH}_4\text{OH}$  (VWR Prolabo Rectapur) were used as starting materials.

**Hydrothermal Synthesis.** According to Beale's conditions of synthesis,<sup>22</sup> two solutions, A (2.32 g of  $\text{Bi}_2\text{O}_3$  dissolved in 5.8 mL of  $\text{HNO}_3$ ) and B (0.88 g of  $(\text{NH}_4)_6\text{Mo}_7\text{O}_{24}\cdot 4\text{H}_2\text{O}$  dissolved in 5.6 mL of aqueous ammonia) were prepared. Solution B was slowly added into solution A. The pH was adjusted with ammonia to be higher than 6, before loading about 1 cm<sup>3</sup> of the solution in the hydrothermal synthesis cell specially designed for *in situ* studies. This cell was introduced into the preheated block just before starting the measurements, which were carried out at 160, 170, and 180 °C.<sup>24</sup> The same procedure was used to prepare samples for *ex situ* experiments, but in larger amounts of the two solutions. After adjustment of the pH, the mixture was loaded into a 20 mL Teflon-lined autoclave, which was introduced in an oven preheated at 180 °C. The experiments were stopped at different times (30 min, 1 h, 1 h 10 min, 1 h 20 min, 1 h 30 min, 2 h, and 20 h), and the autoclave was allowed to cool to room temperature for 2 h. The precipitate was filtered, washed with warm deionized water, and dried in air at room temperature. In one experiment, the precursor was filtered before the reaction in order to identify the sample in the initial stage of reaction.

**Methods.** *In Situ.* Combined X-ray absorption spectroscopy (XAS-XANES), high-resolution powder diffraction (HRPD) and Raman scattering experiments were carried out on the Swiss-Norwegian Beamline (SNBL, BM1B) at the European Synchrotron Radiation Facilities (ESRF) in Grenoble, France, as described in ref 24. XANES (X-ray absorption near-edge spectroscopy) spectra were collected over the photoemission ranges of the molybdenum K edge. They were processed using the Athena graphical interface<sup>26</sup> of the IFEFFIT program suite.<sup>27</sup> High-resolution powder diffraction (HRPD) data were collected at 0.5 Å wavelength in the 8.001–17.514°  $2\theta$  domain with a step of 0.003° and a 150 ms/step counting time. Data were refined with the Fullprof suite.<sup>28</sup> The Thompson–Cox–Hastings pseudo-Voigt profile function was used.<sup>29</sup> The resolution of the instrument was deduced from a  $\text{LaB}_6$  XRD diagram. Raman scattering was carried out on a dispersive InVia Renishaw spectrophotometer with a 532 nm exciting line and 1200 lines/mm grating. A standard Raman RP10 probe with a long-distance objective was connected to the spectrophotometer by optical fibers.<sup>30</sup> Raman spectra were recorded in the 100–1200 cm<sup>−1</sup> range for 132 s with 70 mW laser power. The Labspec program was used for background subtraction and normalization of Raman spectra. XANES and HRPD data were collected sequentially, XANES data over 6 min, followed by HRPD patterns over 7 min, while Raman spectra were recorded continuously during the whole experiment.

*Ex Situ.* Room-temperature XRD analyses were performed with a Bruker AXS D8 Advance diffractometer equipped with a SolX energy-dispersive detector in the 5–80° range (step 0.02°, 2 s/step), using  $\text{Cu K}\alpha$  radiation ( $\lambda = 1.54$  Å). High-temperature X-ray diffraction patterns were performed on a Siemens Bruker D8 diffractometer equipped with an Anton Paar HTK 1200N high-temperature chamber and a one-dimensional detector (Vantec-1). The sample was placed on a Pt foil to protect the alumina plate. The experiments were performed from room temperature to 800 °C with a heating rate of 0.05 °C/s between each diagram, and a diffractogram was recorded every 25 °C, in the 10–70° range in  $2\theta$ , with a step of 0.015° and a counting time of 0.2 s per step. Raman spectra were recorded at room temperature with the

647.1 nm excitation line from a Spectra Physics krypton ion laser with 3 mW laser power. The beam was focused on the samples using the macroscopic configuration. A CCR 1000 Linkam stage was used for study at variable temperatures. The scattered light was analyzed with an XY Raman Dilor spectrometer equipped with an optical multichannel detector (liquid-nitrogen-cooled charge-coupled device). The spectral resolution was approximately 0.5 cm<sup>−1</sup> in the investigated 15–1200 cm<sup>−1</sup> range. A Hitachi S4700 electron microscope with scanning electron microscopy (SEM) and energy-dispersive X-ray spectroscopy (EDS) was used to examine the microstructural features and chemical compositions of synthesized samples.

## 3. RESULTS AND DISCUSSION

**Formation of  $\gamma$ - $\text{Bi}_2\text{MoO}_6$  by Hydrothermal Synthesis (*ex Situ* Study).** The precursor and samples after different times of reaction in a conventional autoclave under hydrothermal conditions were examined by XRD and Raman scattering at room temperature. Stacked XRD patterns are presented in Figure 1. The precursor resulting from mixing

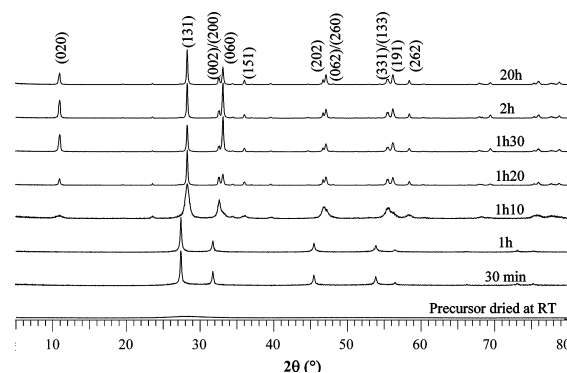


**Figure 1.** XRD powder patterns of the precursor and of samples prepared by the hydrothermal method at 180 °C for various reaction times. In brackets, (*hkl*) of  $\gamma$ - $\text{Bi}_2\text{MoO}_6$  lines.

$\text{Bi}_2\text{O}_3$  and Mo salt was amorphous. An intermediate crystalline phase formed after 30 min. Its XRD pattern was refined in the cubic  $\text{Bi}_2\text{O}_3$  fluorite structure. A good fit was obtained for a cubic cell with  $a = 5.638(4)$  Å. Bismuth only was introduced in the cation site, although the presence of molybdenum could not be excluded (see hereafter). After 1 h 10 min, the Bragg peaks of this phase disappeared while those of  $\gamma$ - $\text{Bi}_2\text{MoO}_6$  started to grow. Pure crystalline  $\gamma$ - $\text{Bi}_2\text{MoO}_6$  (PDF Card 76-2388) was successfully obtained as the final product.

Figure 2 exhibits the Raman spectra evolution for different reaction times. Up to 1 h, the spectral features are practically the same and suddenly change from 1 h 10 min. The four characteristic bands of the  $[\text{MoO}_4]$  tetrahedral species are observed in the precursor, Mo–O stretching motions at 891 and 815 cm<sup>−1</sup>, and O–Mo–O bending motions at 313 and 453 cm<sup>−1</sup>. These wavenumber values are in agreement with the literature data for materials containing tetrahedral molybdates.<sup>31–34</sup> A slight shift of these internal modes toward lower wavenumbers is observed with the progress of the reaction. These observations allow us to conclude that, in the beginning, the Mo environment remains tetrahedral, but with an increase of Mo–O bond lengths.

After 1 h 10 min of reaction, the spectral feature changes; new lines appear at 845, 799, and 718 cm<sup>−1</sup>, which correspond to the stretching motions of distorted  $[\text{MoO}_6]$  in  $\text{Bi}_2\text{MoO}_6$ . In the 270–420 cm<sup>−1</sup> spectral range, where O–Mo–O bending motions are awaited, a splitting in several components leads to

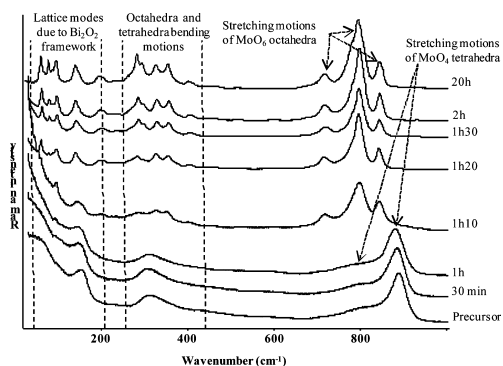


**Figure 2.** Raman spectra of the precursor and of samples prepared by the hydrothermal method at 180 °C for various reaction times.

a better resolution of the spectra and also indicates a phase transition. In the very low wavenumbers, the spectral range of the external lattice modes, a broad weak band at 50  $\text{cm}^{-1}$  disappears after 1 h of reaction while a new weak line appears at 96  $\text{cm}^{-1}$ . Meanwhile, the band at 153  $\text{cm}^{-1}$  in the precursor shifts to 146  $\text{cm}^{-1}$ ; other new lines at 61 and 78  $\text{cm}^{-1}$  and a broad band at 200  $\text{cm}^{-1}$  appear with the formation of  $\gamma\text{-Bi}_2\text{MoO}_6$  at 1 h 20 min of reaction. All of these components can be assigned to the formation of the  $[\text{Bi}_2\text{O}_2]^{2+}$  layers.<sup>35</sup> They are better resolved after 20 h of reaction, which is in agreement with an increase of the crystallite size of the compound. It is worth noting that the line at 96  $\text{cm}^{-1}$ , which appears from 1 h, could indicate the beginning of the transformation of the intermediate fluorite phase into the Aurivillius lattice before the clear observation of  $[\text{MoO}_6]$  species.

Energy-dispersive X-ray spectroscopy (EDS) analyses were performed for all samples (cf. the Supporting Information, Table SI.1). A good homogeneity was noticed for the 1 h 10 min sample, in accordance with XRD patterns, indicating the presence of  $\gamma\text{-Bi}_2\text{MoO}_6$  only. As expected, the Mo stoichiometry was close to the theoretical value of  $\text{Bi}_2\text{MoO}_6$  (ca. 2% of error). For shorter times of reaction, the presence of Mo in the intermediate phase was in a slightly smaller amount than expected ( $\text{Bi}/\text{Mo} = 83.9/16.1$  vs  $81.3/18.7$  for  $\text{Bi}_2\text{MoO}_6$ ). Thus, the  $\text{Bi}_2\text{O}_3$ -type phase was assumed to contain Mo, in the form of a  $(\text{Bi}_{1-x}\text{Mo}_x)_2\text{O}_{3+\delta}$  solid solution ( $x < 0.5$ ), in which the Mo surrounding is tetrahedral. It is worth noting that, in an attempt to prepare the Koechlinite  $\text{Bi}_2\text{MoO}_6$  by precipitation from aqueous solution, Gattow<sup>36</sup> also obtained a cubic form with the fluorite structure that he assigned to a  $\text{Bi}_{1-x}\text{Mo}_x\text{O}_{1.5(1+x)}$  solid solution. However, in his study, analysis of the samples revealed a higher bismuth content than us, which led to a composition close to  $2\text{Bi}_2\text{O}_3\text{-MoO}_3$ . It is also interesting to note that the unit cell parameter he refined ( $a = 5.65 \pm 0.01$  Å) was also close to the value we obtained for the sample after 1 h of reaction ( $a = 5.638(4)$  Å).

To go further in the structural characterization, we recorded an X-ray diffractogram on a wider  $2\theta$  domain ( $25\text{--}130^\circ$ ) with a longer counting time to increase the statistic (step  $0.02^\circ$ , 35 s/step). As written above, a good fit was obtained when only bismuth was introduced in the 4a site of the  $Fm\bar{3}m$  space group of the fluorite structure, but we must also specify that the Bragg peaks' profiles were super-Lorentzian. We managed to obtain a good profile (but not perfect) by introducing a microstrain parameter, but such a particular XRD profile could also possibly be explained by the existence of at least two populations of particles with different crystallite sizes: a strong peak would

characterize the bigger particles, and the broadening at the foot of the peaks would refer to smaller ones. To verify this assumption, TEM was carried out. Despite a lack of stability under the electron beam, micrographs confirmed that particle sizes may be very different and that very small particles were present (cf. the Supporting Information, Figure SI.1). We did carried out several attempts of refinement (one phase with a microstrain parameter, two phases with different crystallite sizes (cf. the Supporting Information, Figure SI.2). Attempts to introduce molybdenum in the 4a site led to negative occupancy for this atom, but with such uncertainties on the profile and the limited number of Bragg peaks, we think the limit of powder diffraction is reached and it is difficult to conclude about the molybdenum occupancy in this site. Moreover, as Gattow<sup>36</sup> did, we introduced all oxygen atoms in the 8c site of the fluorite structure. It is worth noting that an increase of oxygen occupancy led to an increase of reliability factors, which was higher than the introduction of molybdenum in the bismuth site only. Because of the expected shorter Mo–O bond length, compared to the Bi–O bond length, as already shown for other fluorite structures,<sup>37</sup> oxygen is likely distributed on several sites to allow a local tetrahedral environment for molybdenum. Refinement of oxygen occupancy led to divergence. Using X-ray diffraction only, because of the low scattering factor of oxygen compared with that of bismuth, an accurate location of oxygen is difficult and would need the addition of neutron diffraction data. Calculated profiles compared to experimental data are given in the Supporting Information (cf. Figure SI.2). Introduction of molybdenum with its expected occupancy and increasing oxygen occupancy accordingly led to slightly higher reliability factors, but this does not contradict the possibility of molybdenum in this site. Interestingly, an analysis of the evolution of the full width at half-maximum of Bragg peaks according to the Williamson and Hall plots<sup>38</sup> for the X-ray pattern collected after 30 min and 1 h of reaction led to particle sizes of 50 and 80 nm, respectively, and microstrains of 0.2% and 0.4%, respectively (cf. the Supporting Information, Figure SI.3).

Figure 3 shows SEM images of the precursor and of precipitates for various times of hydrothermal reaction. The particle shape of the precursor and of the intermediate fluorite phase was nearly spherical, about 50 nm in diameter. The first particles of  $\gamma\text{-Bi}_2\text{MoO}_6$ , which appeared after 1 h 10 min of reaction, displayed irregular disk shapes with variable sizes. In a short time (10 min), they transformed into irregular plates that were about 3 times larger. These platelets grew slowly upon increasing the reaction time, in agreement with XRD analyses, which showed highly broadened profiles for the 1 h 10 min sample (Figure 1).

The synthesis of bismuth molybdates was reported to be extremely dependent on the pH value.<sup>39</sup> Here, according to Beale's results,<sup>22</sup> the pH was fixed to be higher than 6. To go further in the understanding of  $\gamma\text{-Bi}_2\text{MoO}_6$ , solutions of ammonium heptamolybdate tetrahydrate dissolved in ammonia, with the pH adjusted at 1, 4, 6, 7, and 10 by addition of nitric acid, were analyzed by Raman scattering (cf. the Supporting Information, Figure SI.4). The extra lines observed at 720 and 1050  $\text{cm}^{-1}$  correspond, respectively, to the symmetrical bending and stretching vibrations of the  $\text{NO}_3^-$  anion in nitric acid solution. It was found that, at  $\text{pH} > 6$ , only  $[\text{MoO}_4]^{2-}$  tetrahedra, with the characteristic bands at 319, 842, and 898  $\text{cm}^{-1}$ , are present in the solution. At lower pH, the formation of other polyoxomolybdates, such as  $[\text{Mo}_7\text{O}_{24}]^{6-}$ ,



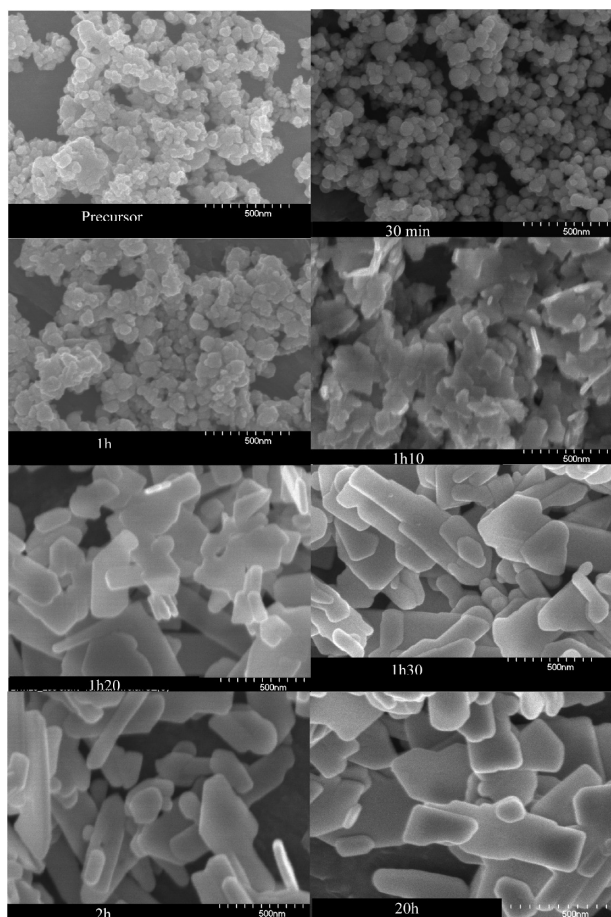


**Figure 3.** SEM images of the precursor and of samples prepared hydrothermally at 180 °C for various reaction times.

$[\text{HMo}_7\text{O}_{24}]^{5-}$ , or  $[\text{Mo}_{36}\text{O}_{112}]^{8-}$ , was observed (cf. the Supporting Information, Table SI.2). The pH dependence of the observed species is in good agreement with the literature.<sup>33–35</sup> Consequently, the formation of the pure crystallized  $\gamma\text{-Bi}_2\text{MoO}_6$  from a gel at pH > 6 is obviously related to the necessity of the monomeric molybdates,  $[\text{MoO}_4]^{2-}$ , in the precursor.

As a partial conclusion, this ex situ study confirmed the two-step mechanism proposed after in situ experiments.<sup>24,25</sup> In addition, isotropic particles of  $(\text{Bi}_{1-x}\text{Mo}_x)_2\text{O}_{3+\delta}$  solid solution as the intermediate phase were put in evidence, before the growing of highly anisotropic platelets of  $\gamma\text{-Bi}_2\text{MoO}_6$  in the second step. The Mo surrounding in the intermediate form is tetrahedral, in good agreement with the pH value required for the synthesis, which corresponds to monomeric  $[\text{MoO}_4]^{2-}$  molybdates in solution.

#### In Situ Combined HRPD/XAS/Raman Experiments.

The synthesis of  $\gamma\text{-Bi}_2\text{MoO}_6$  under hydrothermal conditions, followed in situ by combined HRPD/XAS/Raman techniques, was carried out at 160, 170, and 180 °C.<sup>24,25</sup> Whatever the temperature, a two-step reaction was found, as confirmed by the ex situ study just described. At 160 °C, for example, HRPD patterns showed wide peaks of a crystalline phase appearing from the very first minutes. During the course of the reaction, this intermediate gradually transformed into  $\gamma\text{-Bi}_2\text{MoO}_6$ . XRD refinement was applied to determine the structure and morphology of the nucleating intermediate phase.<sup>24</sup> Unlike ex situ experiments, in which the symmetry of the intermediate

form appeared to be cubic ( $Fm\bar{3}m$ ), here, a good profile was only obtained when taking into account a tetragonal distortion. The structure could be viewed as a distorted fluorite structure compressed along the [001] direction. The XRD refinement, taking into account the line broadening by using fwhm values, revealed the formation of spherical particles of  $\text{Bi}_2\text{O}_3$ -type, in agreement with ex situ SEM images up to 1 h (Figure 3).

The  $\gamma\text{-Bi}_2\text{MoO}_6$  structure was refined using the structural model proposed by Theobald et al.<sup>14</sup> in the  $Pca2_1$  space group. As an anisotropic broadening of Bragg peaks was observed, a linear combination of spherical harmonics of the fourth order was used together with the Scherrer formula.<sup>40</sup> In good agreement with ex situ SEM results, the refinement revealed the platelet shape of the  $\gamma\text{-Bi}_2\text{MoO}_6$  crystallites. The very small thickness along the [010] direction<sup>24</sup> led to a lack of accuracy for the  $b$  parameter in the initial stage of the reaction.

In the 35–120 min range, during which the two phases coexisted, the refined  $a$  and  $c$  cell parameters of the orthorhombic  $\text{Bi}_2\text{MoO}_6$  structure were found to gradually decrease upon increasing the time. It was worth to note that, by extrapolation to the time close to zero,  $a$  and  $c$   $\text{Bi}_2\text{MoO}_6$  converged to  $c_F$  and  $a_F$   $\text{Bi}_2\text{O}_3$  values of distorted fluorite, respectively, suggesting that the formation of  $\gamma\text{-Bi}_2\text{MoO}_6$  particles would start from  $\text{Bi}_2\text{O}_3$ -type crystallites.<sup>25</sup>

The structural modifications around molybdenum during the reaction was observed by the complementary Mo K-edge XANES and Raman spectroscopy techniques.<sup>24,25</sup> The interpretation of XANES was based on the relative intensity of the pre-edge peak at ca. 19987 eV related to the 1s–4d transition, and of the shoulder on the top of the edge, related to the 1s–5p transition at ca. 20006 eV (Figure 4). The spectra of

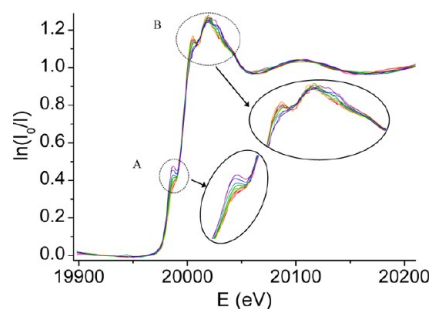


**Figure 4.** Mo K-edge XANES spectra collected at 160 °C showing isosbestic points (in situ experiments). The features marked A and B are characteristic of Mo(VI) in tetrahedral and octahedral environments, respectively.

the precursor displayed a strong pre-edge peak and a weak shoulder on the top of the edge, which suggested the presence of noncentrosymmetric tetrahedral  $[\text{MoO}_4]$  species.<sup>20,41</sup> After ca. 40 min of reaction, the pre-edge intensity decreased and the intensity of the shoulder on the top of the edge increased, accounting for the conversion of tetrahedral to octahedral coordination around Mo. This observation was consistent with a previous study by XAS/HRXRD performed on the same system, but at lower temperatures (120–150 °C).<sup>20,23</sup> Moreover, isosbestic points were also evidenced (Figure 4), which would indicate that (i) the two chemical species  $[\text{MoO}_4]$  and  $[\text{MoO}_6]$  have identical molar absorption coefficients, which remain constant as the reaction proceeds, and (ii) the reaction is probably a direct transformation from  $[\text{MoO}_4]$  to  $[\text{MoO}_6]$  species.

Raman scattering also probed the change of Mo coordination, whose spectral feature differs for tetrahedral or octahedral species. In situ spectra were very similar to those obtained ex situ, with the exception of the low-frequency range, whose modifications are likely due to a pressure effect, as shown by Maczka et al.<sup>42</sup> Interestingly, a  $16\text{ cm}^{-1}$  shift of the tetrahedral  $[\text{MoO}_4]$  main Raman line  $\nu_1(\text{A}_1)$  toward low wavenumbers was observed during the first 20 min of reaction (Figure 5),

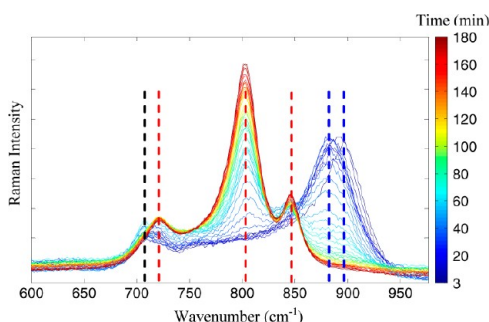


**Figure 5.** Raman spectra in the range of  $600\text{--}975\text{ cm}^{-1}$ , showing the transformation from  $[\text{MoO}_4]$  (characteristic band in dashed blue lines) to  $[\text{MoO}_6]$  in  $\gamma\text{-Bi}_2\text{MoO}_6$  (characteristic bands in dashed red lines).

characterizing an elongation of the Mo–O bonds. In addition, we can note that, during the transformation of  $[\text{MoO}_4]$  into  $[\text{MoO}_6]$ , no wavenumber shift is observed for the main characteristic lines of the two species.

For a better understanding of this phenomenon, the evolution of the wavenumber of the  $[\text{MoO}_4]$  stretching mode on one side and the change in the relative abundance of molybdate species from XANES data on the other side were plotted against time at  $160^\circ\text{C}$  (Figure 6). This plot revealed a

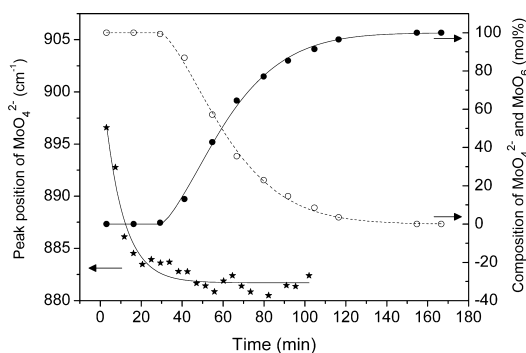


**Figure 6.** Plots of the positional shift of the  $\text{MoO}_4^{2-}$  Raman band (★) and the composition of  $\text{MoO}_4^{2-}$  (○) and  $\text{MoO}_6$  (●) species (from XANES spectra) during the hydrothermal synthesis of  $\gamma\text{-Bi}_2\text{MoO}_6$  at  $160^\circ\text{C}$ .

change of the  $[\text{MoO}_4]$  tetrahedral species before they transform into  $\text{MoO}_6$  octahedra as in the  $\gamma\text{-Bi}_2\text{MoO}_6$  structure, characterized by the elongation of Mo–O bonds that may be caused by the interaction between the positively charged  $[\text{Bi}_2\text{O}_2]^{2+}$  layers and the negatively charged  $[\text{MoO}_4]^{2-}$  entities.

**Kinetics of Crystallization.** To derive kinetic information for the transformation of tetrahedral  $[\text{MoO}_4]$  into octahedral  $[\text{MoO}_6]$  in  $\gamma\text{-Bi}_2\text{MoO}_6$ , a linear combination fitting (LCF) analysis was carried out on both XANES and Raman scattering to quantify these two molybdate species. Although the

transformation of Mo species could be better resolved with a shorter acquisition time of Raman spectra (a Raman spectrum was collected every 2 min, whereas a XANES spectrum was collected every 13 min), the quantitative Raman spectroscopy technique had to be calibrated or validated by the XANES technique. Three assumptions were made. First,  $[\text{MoO}_6]$  species were considered to be absent before the evolution of  $[\text{MoO}_4]$  species was completed. Second, the first spectrum collected just after the stabilization of  $[\text{MoO}_4]$  species and the last spectrum collected at the end of each reaction were those of only  $[\text{MoO}_4]$  and only  $[\text{MoO}_6]$ , respectively (and used as reference spectra). Third, because of the direct transformation of  $[\text{MoO}_4] \rightarrow [\text{MoO}_6]$ , only four and six coordinate molybdenum were considered. Linear combinations of these reference spectra were used to construct a model spectrum, and their proportion was refined by using a least-squares fitting algorithm to minimize the difference between the model and the experimental spectra. LCF analysis was applied on the normalized XANES spectra in the  $-40\text{ eV} < E_0 < 30\text{ eV}$  range, the Athena software was used,<sup>26</sup> and a good fit was obtained ( $R$  factor  $< 0.0004$ ). For Raman spectra, the multiple regression function in the Matlab program was used in the  $600\text{--}975\text{ cm}^{-1}$  range. A good fit between the calculated and experimental spectra was obtained (cf. the Supporting Information, Figure SI.5). The abundance of  $[\text{MoO}_4]$  and  $[\text{MoO}_6]$  species deduced from both Raman and XANES data was plotted as a function of time for the three temperatures ( $160$ ,  $170$ , and  $180^\circ\text{C}$ ) (cf. the Supporting Information, Figure SI.6). The average deviation between the two techniques was within 3 min for  $[\text{MoO}_6]$  compositions smaller than 80%, and can be explained by the lack of time accuracy for XANES spectra (collected for 6 min every 13 min). From Rietveld refinement of XRD data, the molar fraction value of  $\gamma\text{-Bi}_2\text{MoO}_6$  and hence of  $[\text{MoO}_6]$  species was also derived. It is compared to the  $\text{MoO}_6$  composition obtained from both XANES and Raman scattering at  $180^\circ\text{C}$  in Figure 7. Since the correlation obtained by the

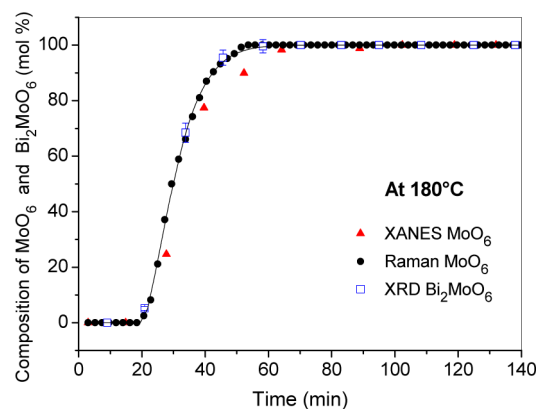


**Figure 7.** In situ analyses during the hydrothermal synthesis of  $\gamma\text{-Bi}_2\text{MoO}_6$  at  $180^\circ\text{C}$ . Evolution of  $\text{MoO}_6$  content (XANES: red ▲; Raman: black ●), and of  $\text{Bi}_2\text{MoO}_6$  content obtained from XRD (blue □).

three techniques was rather good, Raman data were considered as reliable and, consequently, were used to determine the crystallization mechanisms of  $\gamma\text{-Bi}_2\text{MoO}_6$ .

The sigmoidal curves are typical of a crystallization process consisting of (i) an initial induction time ( $t_{\text{ind}}$ ), followed by (ii) a slow growth of initial nuclei before (iii) a rapid transformation into  $\text{Bi}_2\text{MoO}_6$  particles, until all the reactant is consumed. As

expected, the reaction was faster when the temperature was increased. The growth of  $\text{Bi}_2\text{MoO}_6$  at 160, 170, and 180 °C took about 100, 75, and 60 min, respectively, to reach completion.

The kinetic model of Johnson–Mehl–Avrami<sup>43–46</sup> has been widely used for analyzing solid crystallization and phase transformations. Its equation (eq 1) states that the extent of reaction ( $\alpha$ ) in time ( $t$ ) is related to the rate constant ( $k$ ) and the Avrami exponent ( $n$ ):

$$\alpha = 1 - \exp[-(kt)^n] \quad (1)$$

It is worth noting that ( $t$ ) refers to the time after an induction period ( $t_{\text{ind}}$ ). In our case, the extent of reaction ( $\alpha$ ) at each temperature was obtained through the normalization of the  $\gamma\text{-Bi}_2\text{MoO}_6$  contents monitored by in situ Raman spectroscopy (cf. the Supporting Information, Figure SI.7). The values were plotted against the reaction time ( $t$ ) according to the Sharp–Hancock equation (eq 2):<sup>47</sup>

$$\ln[-\ln(1 - \alpha)] = n \ln k + n \ln t \quad (2)$$

Linear plots of  $\ln[-\ln(1 - \alpha)]$  against  $\ln(t - t_{\text{ind}})$  were obtained at each temperature. The Sharp–Hancock analysis was performed for  $\alpha$  values from 0.15 to 0.80, because the results obtained from the three different techniques (XRD, XANES, and Raman spectroscopy) are the most reliable and coherent in this range. The resulting three linear Sharp–Hancock plots (Figure 8) confirmed the validity of the nuclei

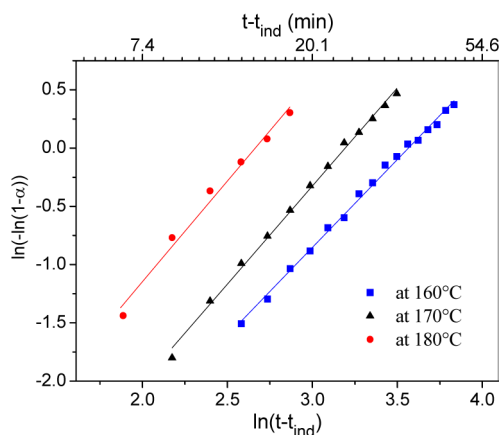


**Figure 8.** Sharp–Hancock plots for the  $0.15 < \alpha < 0.80$  data range recorded at various reaction temperatures.

growth model. They confirmed as well that the reaction mechanism did not change in the  $\alpha$  range studied. The Avrami exponent ( $n$ ) (from the slope) and rate constant ( $k$ ) (from the intercept) are gathered in Table 1. The values of  $n = 1.5$ – $1.8$  accounting for both nucleation and growth are typical of a 2D-

**Table 1.** Avrami Exponents ( $n$ ) and Rates of Crystallization ( $k$ ) As Derived from Sharp–Hancock Analysis

temp (°C)	$n$	$k$ ( $\text{min}^{-1}$ )	$R^2$ factor	ref
110	1.06	0.0270		22
140	1.19	0.0471		22
150	0.97	0.0634		22
160	1.51	0.0283	0.9966	this work
170	1.68	0.0410	0.9969	this work
180	1.73	0.0697	0.9859	this work

growth process limited by diffusion, with decreasing nucleation rate.<sup>48</sup> Beale et al.<sup>20,22,23</sup> already proposed this mechanism for the same system at lower temperatures (110–150 °C) (Table 1). The activation energy, obtained from the Arrhenius equation by plotting  $\ln(k)$  against  $1/T$ , was  $72(9) \text{ kJ mol}^{-1}$ . The 2D-growth mechanism is in accordance with the platelet morphology of  $\gamma\text{-Bi}_2\text{MoO}_6$ , revealed by XRD refinement and ex situ SEM images, which, in turn, is related to the Aurivillius structure.

#### Comparison between in Situ and ex Situ Experiments.

The rates of in situ and ex situ reactions were somewhat different. At 180 °C, ex situ discontinuous experiments showed that the transformation  $\text{Bi}_2\text{O}_3$ -type  $\rightarrow \gamma\text{-Bi}_2\text{MoO}_6$  lasted 20 min and that the formation of  $\gamma\text{-Bi}_2\text{MoO}_6$  started after 1 h 10 min, compared to longer transformation (40 min) and faster formation (22.8 min) times for in situ experiments, respectively. These time shifts are likely due to the high thermal inertia of the conventional autoclave while heating and cooling. During the transformation, the reaction likely continues to proceed during the slow cooling stage. For short experiments, samples may not reach the desired temperature. This underlines the importance of in situ experiments to extract accurate information on the kinetics.

Though not so important in the case of the final product,  $\gamma\text{-Bi}_2\text{MoO}_6$ , as far as the platelet morphology of bismuth molybdate was considered (Figure 3), the ex or in situ conditions had an influence on the symmetry of the intermediate  $\text{Bi}_2\text{O}_3$ -type. As determined from HRPD measurements, the symmetry was tetragonal and its structure was viewed as a distorted fluorite compressed along the [001] direction. At variance, a cubic symmetry was evidenced for ex situ samples, as if the fluorite structure was under strain due to autogenous pressure during in situ experiment.

**Light on the Intermediate Compound.** The in situ study clearly shows that crystals of  $\gamma\text{-Bi}_2\text{MoO}_6$  are nucleated from an intermediate distorted fluorite structure related to  $\text{Bi}_2\text{O}_3$ . However, at this stage, some points remain uncertain. What is the exact composition of the intermediate form? Does it contain any molybdenum in the structure?

According to XRD, Raman scattering (Figures 1 and 2) and EDS experiments (cf. the Supporting Information, Table SI.1), Mo tetrahedral species appeared to be incorporated in the  $\text{Bi}_2\text{O}_3$ -type intermediate as a  $(\text{Bi}_{1-x}\text{Mo}_x)_2\text{O}_{3+\delta}$  solid solution. In such a case, this compound should transform to one or more known phases of the Bi–Mo–O system upon heating. To verify this assumption, thermogravimetric analysis and differential thermal analysis combined with analysis of released gases by mass spectrometry were carried out on the 1 h ex situ sample (in air, up to 800 °C; cf. the Supporting Information, Figure SI.8).

Below 460 °C, two weight losses were accounted for by the loss of water ( $\sim 1.1\%$  up to 209 °C), and nitrate decomposition ( $\sim 0.28\%$  between 209 and 460 °C), as revealed by the formation of water and NO, respectively. A very small loss of weight ( $< 0.1\%$ ) was observed, which corresponded to a large broad exothermic DTA signal at 427 °C. While the weight remained the same, two small endothermic signals at 670 and 690 °C during heating and a small exothermic signal at 348 °C on cooling were also noticed. As these signals might indicate phase transformations, high-temperature XRD and Raman spectroscopy at variable temperature were carried out.

High-temperature XRD (Figure 9) showed that the initial fluorite structure observed at room temperature was stable up



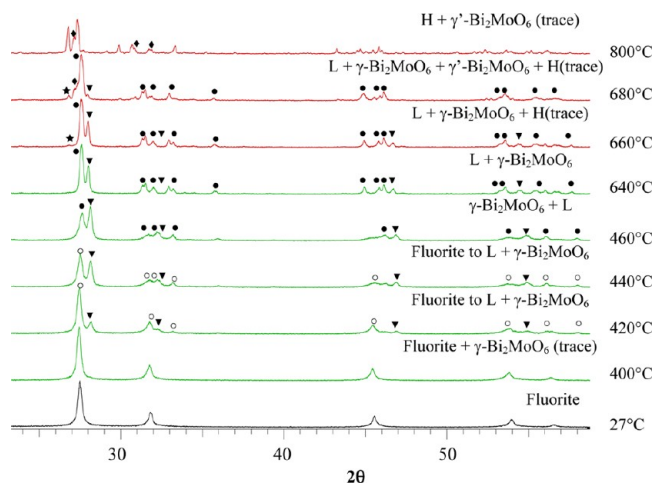
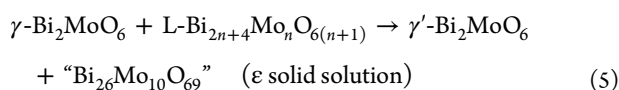
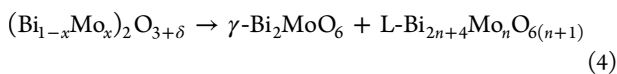
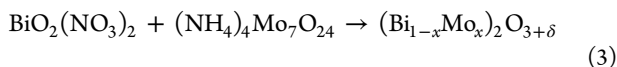


**Figure 9.** XRD patterns of the sample taken after 1 h of reaction (hydrothermal cell) vs temperature in air (27–800 °C): (○) fluorite, (●)  $\text{L-Bi}_{2n+4}\text{Mo}_n\text{O}_{6(n+1)}$ , (▼)  $\gamma\text{-Bi}_2\text{MoO}_6$ , (★)  $\text{H-Bi}_{2n+4}\text{Mo}_n\text{O}_{6(n+1)}$  ( $\epsilon$  solid solution), (◆)  $\gamma'\text{-Bi}_2\text{MoO}_6$ .

to 400 °C. The final XRD pattern at 800 °C revealed the presence of two phases,  $\gamma'\text{-Bi}_2\text{MoO}_6$  (high-temperature polymorph of  $\gamma\text{-Bi}_2\text{MoO}_6$ )<sup>49</sup> and a member of the  $\epsilon$  solid solution,  $\text{Bi}_{26}\text{Mo}_{10}\text{O}_{69}$ .<sup>50,51</sup> The homogeneity range of  $\epsilon$  was  $27.75/10 \leq \text{Bi}/\text{Mo} \leq 25.75/10$ ; this result confirmed EDS experiments, showing that the Bi content was slightly higher than that in  $\text{Bi}_2\text{MoO}_6$  for samples obtained at reaction times shorter than 1 h. Between 400 and 600 °C, two phase transformations were observed. At 420 °C, a thorough examination of the XRD pattern revealed that, besides the lines of  $\gamma\text{-Bi}_2\text{MoO}_6$ , a compound of the  $\text{L-Bi}_{2n+4}\text{Mo}_n\text{O}_{6(n+1)}$  series (L for low temperature) was present.<sup>52</sup> From 460 to 640 °C, the intensity of  $\gamma\text{-Bi}_2\text{MoO}_6$  lines decreased upon increasing temperature, while lines of  $\text{Bi}_{2n+4}\text{Mo}_n\text{O}_{6(n+1)}$  became stronger. However, at 640 °C,  $\gamma\text{-Bi}_2\text{MoO}_6$  did not totally transform into  $\text{Bi}_{2n+4}\text{Mo}_n\text{O}_{6(n+1)}$ , which was likely due to the higher amount of Mo in our sample as compared with  $\text{Bi}_{2n+4}\text{Mo}_n\text{O}_{6(n+1)}$ . It is worth noting that these phase transitions correlated well with the two small endothermic signals located at 670 and 690 °C on the DTA curve. Above 660 °C, the phase transition to  $\gamma'\text{-Bi}_2\text{MoO}_6$  (the high-temperature form of  $\text{Bi}_2\text{MoO}_6$ ) happened, just before the conversion of  $\text{Bi}_{2n+4}\text{Mo}_n\text{O}_{6(n+1)}$  into an  $\epsilon$ -type structure ( $\text{H-Bi}_{2n+4}\text{Mo}_n\text{O}_{6(n+1)}$ ).

Thus, upon heating, the fluorite intermediate was transformed to  $\gamma\text{-Bi}_2\text{MoO}_6$  and  $\text{L-Bi}_{2n+4}\text{Mo}_n\text{O}_{6(n+1)}$ , which, in turn, were transformed to  $\gamma'\text{-Bi}_2\text{MoO}_6$  and  $\epsilon$  solid solution according to the following reactions:



These phase transitions were confirmed by Raman spectroscopy (Figure 10). Almost no modification of the spectrum was observed up to 400 °C, in good agreement with X-ray diffraction. A shift of the band assigned to the symmetrical stretching motion  $\gamma_1(\text{A}_1)$  in  $[\text{MoO}_4]$  tetrahedra from 883  $\text{cm}^{-1}$

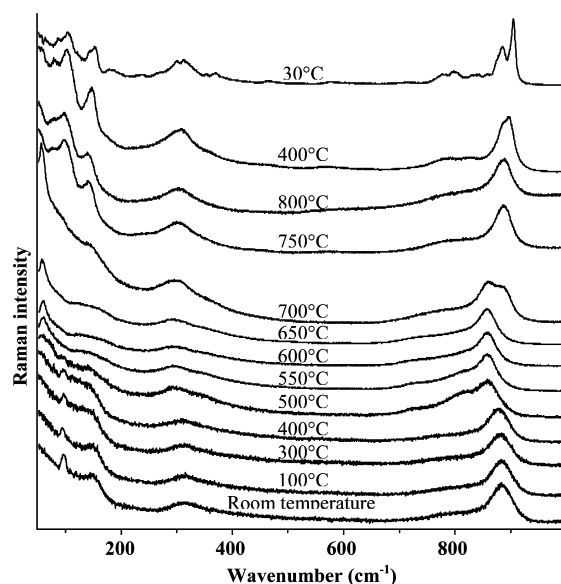


**Figure 10.** Raman spectra collected at variable temperatures in air on the sample taken after 1 h of reaction at 180 °C (hydrothermal cell, ex situ experiment).

at room temperature, to 877  $\text{cm}^{-1}$  at 400 °C and 858  $\text{cm}^{-1}$  at 500 °C, was accompanied with an increase in intensity of the band located at 812  $\text{cm}^{-1}$ . These features are in good agreement with the mixture of  $\text{L-Bi}_{2n+4}\text{Mo}_n\text{O}_{6(n+1)}$  and  $\gamma\text{-Bi}_2\text{MoO}_6$  at 500 °C revealed by XRD. From 500 to 650 °C, only the decrease of intensity of the characteristic Raman bands of  $\gamma\text{-Bi}_2\text{MoO}_6$  was noticed, indicating the transformation from  $\gamma\text{-Bi}_2\text{MoO}_6$  to  $\text{L-Bi}_{2n+4}\text{Mo}_n\text{O}_{6(n+1)}$ . At ca. 700 °C, a new band at 886  $\text{cm}^{-1}$  appeared with the formation of  $\gamma'\text{-Bi}_2\text{MoO}_6$  and an  $\epsilon$ -type structure ( $\text{H-Bi}_{2n+4}\text{Mo}_n\text{O}_{6(n+1)}$ ) that had been evidenced by X-ray diffraction. This Mo–O stretching vibration band occurs at almost the same position as that of the unheated intermediate compound, which would indicate that  $[\text{MoO}_4]$  tetrahedra in these three structures could have a similar local structure. Interestingly, the structures of these two compounds derive from the fluorite structure and are built upon Bi–O columns of fluorite type spaced with  $[\text{MoO}_4]$  tetrahedra.<sup>46–48</sup> This is a further evidence of the validity of the proposed structure of the intermediate form, which likely corresponds to a Bi–O fluorite network with  $[\text{MoO}_4]$  species randomly distributed inside.

The shift of the band assigned to the symmetrical stretching vibration  $\nu_1(\text{A}_1)$  in  $[\text{MoO}_4]$  tetrahedra at 500 °C is also of interest, and it can be compared to the shift of the same band at the initial stage of the transformation of the intermediate form during the in situ investigation.

This high-temperature study gives new insight in the formation of  $\gamma\text{-Bi}_2\text{MoO}_6$ , and the structure of the  $\text{L-Bi}_{2n+4}\text{Mo}_n\text{O}_{6(n+1)}$  may provide the missing element in the understanding of  $\gamma\text{-Bi}_2\text{MoO}_6$  formation.

The structure of  $\text{L-Bi}_{2n+4}\text{Mo}_n\text{O}_{6(n+1)}$  compounds ( $n = 3\text{--}6$ ) was recently determined by HREM, neutron, and X-ray diffractions experiments.<sup>53</sup> It can be viewed as a stack of  $[\text{Bi}_{2n+4}\text{O}_{2n+6}]^{2n+}$  layers that run parallel to the (001) plane, surrounded by groups of  $n$  isolated  $[\text{MoO}_4]$  tetrahedra (Figure 11). These  $n$   $\text{MoO}_4$  groups are inserted into channels along [010], and bordered by Bi 6s<sup>2</sup> lone pairs. Although  $\gamma\text{-Bi}_2\text{MoO}_6$  is made of corner-sharing  $\text{MoO}_6$  octahedra, it could be viewed as the  $n = \infty$  of this series. The distortion of Mo octahedra in

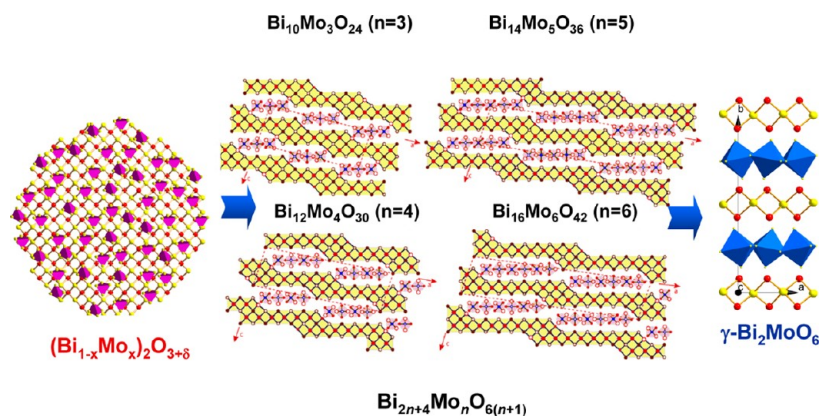


**Figure 11.** Schematics of the successive transformations during the formation of  $\gamma$ - $\text{Bi}_2\text{MoO}_6$ .

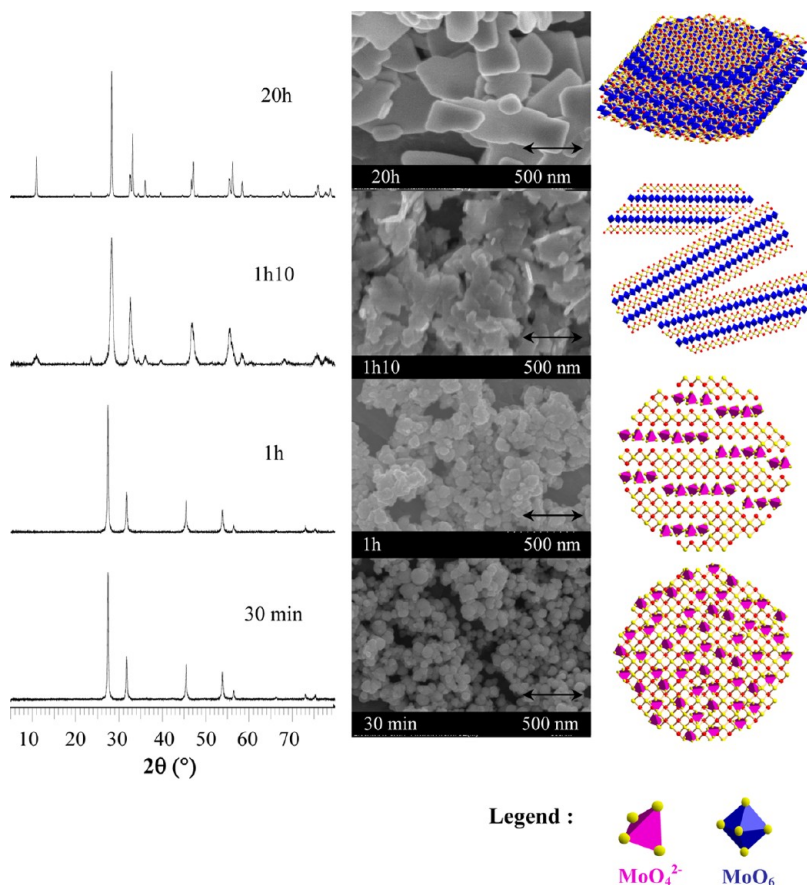


**Figure 12.** XRD patterns, SEM images, and proposed atomic-level models of samples prepared by hydrothermal synthesis at 180 °C, for (from bottom to top) 30 min, 1 h, 1 h 30 min, and 20 h.

the latter is likely due to the  $6s^2$  lone pair of Bi perturbing the tetrahedral coordination of the Mo atom. Indeed, at variance, symmetric  $[\text{MoO}_4]$  tetrahedra are found in the  $\text{La}_2\text{MoO}_6$  structure,<sup>54</sup> though it is similar to that of  $\gamma$ - $\text{Bi}_2\text{MoO}_6$ . Therefore, the relationship between  $\gamma$ - $\text{Bi}_2\text{MoO}_6$  and  $\text{L-Bi}_{2n+4}\text{Mo}_n\text{O}_{6(n+1)}$  is as well demonstrated by the similarity between the high-temperature forms,  $\gamma'$ - $\text{Bi}_2\text{MoO}_6$  and the  $\epsilon$ -type solid solution. On the basis of these similarities, a scenario for the formation of  $\gamma$ - $\text{Bi}_2\text{MoO}_6$  can be proposed.

#### Proposed Scenario for the Formation of $\gamma$ - $\text{Bi}_2\text{MoO}_6$ .

From both in situ and ex situ studies, the following features were evidenced:

- (1) A fluorite-type structure forms in the first minutes of reaction.
- (2) This solid solution is slightly richer in bismuth than the target  $\text{Bi}_2\text{MoO}_6$  composition, as evidenced by EDS analysis.
- (3) The presence of Mo in the solid was confirmed by EDS analysis of powder prepared ex situ and high-temperature X-ray diffraction and Raman spectroscopy. It likely forms a  $(\text{Bi}_{1-x}\text{Mo}_x)_2\text{O}_{3+\delta}$  solid solution with bismuth oxide.
- (4) The pH dependence of molybdate entities in solution confirmed the necessity of monomeric molybdate species,  $[\text{MoO}_4]^{2-}$ , in the precursor to allow the formation of  $\gamma$ - $\text{Bi}_2\text{MoO}_6$ .



- (5) In the first stage of the reaction, a shift of the band assigned to the symmetrical stretching mode  $\nu_1(A_1)$  in  $[\text{MoO}_4]$  tetrahedra was observed toward lower wavenumbers, indicating a modification of  $[\text{MoO}_4]$  tetrahedra due to an increase of Mo–O bond lengths in the  $[\text{MoO}_4]$ , which stabilizes once it starts to transform into  $[\text{MoO}_6]$  species.
- (6) This shift in wavenumber can be compared to the shift observed for the same band on the 1 h ex situ sample when it transforms to a mixture of  $\text{L-Bi}_{2n+4}\text{Mo}_n\text{O}_{6(n+1)}$  and  $\gamma\text{-Bi}_2\text{MoO}_6$  upon heating at 500 °C.
- (7) The line located at 96  $\text{cm}^{-1}$  on ex situ Raman spectra appears from 1 h, which indicates the beginning of the transformation of the intermediate fluorite phase into the Aurivillius lattice before the clear observation of  $[\text{MoO}_6]$  species.
- (8) Kinetics analysis of experimental data versus time during in situ experiments confirmed a 2D-growth process limited by diffusion.

On the basis of these conclusions, a model can be proposed (Figure 12). First, a distorted fluorite structure, in which  $\text{MoO}_4$  species are randomly distributed, forms. As the reaction time increases, these species (both  $[\text{Bi}_2\text{O}_2]$ -type and  $[\text{MoO}_4]$ ) would self-organize, in a similar way as in the  $\text{L-Bi}_{2n+4}\text{Mo}_n\text{O}_{6(n+1)}$  structure. This organization would consist of the formation of a structure related to that of  $[\text{Bi}_{2n+4}\text{O}_{2n+6}]^{2n+}$  layers intercalated with isolated  $[\text{MoO}_4]$  tetrahedra randomly distributed in the fluorite network, leading to an average fluorite structure, as evidenced by X-ray diffraction. Later, the spherical particle of fluorite would explode into small strips, as shown by SEM, which will serve as germs for the growth of  $\gamma\text{-Bi}_2\text{MoO}_6$  particles. Finally, these thin platelets would further grow into well-crystallized layered crystals of  $\gamma\text{-Bi}_2\text{MoO}_6$ , as supported by XRD and SEM, shown in Figure 12.

#### 4. CONCLUSION

This paper presents an extensive ex situ study using XRD, Raman scattering, EDS, HTXRD, and HT Raman scattering, which allowed us to complete and confirm the results formerly obtained by in situ study, and also to propose a scenario of the growth of  $\gamma\text{-Bi}_2\text{MoO}_6$  crystals. In addition, for the first time, we compared the kinetic analysis from three different characterization techniques. XAS and Raman spectroscopy probe the reaction occurring around the molybdenum atom, whereas HRPD monitors the transformation of the crystalline structure. By combining these results with complementary ex situ studies (HTXRD, Raman scattering, SEM/EDX), it was possible to elucidate the nature of the intermediate phase and the mechanism of  $\gamma\text{-Bi}_2\text{MoO}_6$  formation. Consequently, a tentative scenario of  $\gamma\text{-Bi}_2\text{MoO}_6$  formation was proposed. A distorted fluorite structure, in which  $[\text{MoO}_4]$  species are randomly distributed, forms in the initial stage of the reaction, in agreement with the need of  $[\text{MoO}_4]^{2-}$  species in the solution. These species may then self-organize, in a similar way as in  $\text{L-Bi}_{2n+4}\text{Mo}_n\text{O}_{6(n+1)}$ , before explosion into small strips that will serve as germs for the growth of  $\gamma\text{-Bi}_2\text{MoO}_6$  particles. Here, techniques were pushed to their limits, mainly X-ray powder diffraction. We are almost convinced that a  $(\text{Bi}_{1-x}\text{Mo}_x)_2\text{O}_{3+\delta}$  solid solution forms during the first minutes of reaction; however, because of complex X-ray diffraction data due to samples with different grain sizes and possible microstrain, we did not manage to confirm the introduction of molybdenum in

the bismuth site of the fluorite structure, nor the actual oxygen atoms' location in the structure. EXAFS is currently in progress, and we expect to derive more information on the second sphere of coordination of Mo atoms. Despite the problem with different size populations, neutron diffraction should also give additional information, at least for the oxygen atoms' location.

This study demonstrates the power of a multitechnique approach combining both in situ and ex situ characterizations for the understanding of the crystal growth under hydrothermal conditions, which may help in the design of new materials.

#### ■ ASSOCIATED CONTENT

##### Supporting Information

Bi and Mo contents in samples after hydrothermal synthesis at 180 °C for different times, obtained from energy-dispersive X-ray spectroscopy (EDS) analyses; TEM images of the samples prepared by hydrothermal method at 180 °C for 1 h; Results of Rietveld refinement of the X-ray data collected on the powder after 1 h of reaction under hydrothermal condition at 180 °C; polyoxomolybdates in aqueous solutions and their corresponding Raman bands; Raman spectra of ammonium heptamolybdate tetrahydrate dissolved in ammonia, with pH adjusted by addition of nitric acid at 1, 4, 6, 7, and 10 compared to the spectra of  $(\text{NH}_4)_6\text{Mo}_7\text{O}_{24}\cdot 4\text{H}_2\text{O}$ ,  $\text{Bi}_2\text{MoO}_6$  gel after 3 min of reaction (in situ) and  $\text{Bi}_2\text{MoO}_6$  gel after 186 min at 160 °C (in situ); comparison between Raman spectra and calculated spectra from LCF after 29.4, 42.6, 60.2, 77.8, and 183.5 min of reaction at 160 °C; in situ analyses during the hydrothermal synthesis of  $\gamma\text{-Bi}_2\text{MoO}_6$  at 160–180 °C; extent of reaction versus time, monitored by in situ Raman spectroscopy at 160, 170, and 180 °C; and combined TGA/DTA/MS analyses carried out on the sample taken after 1 h of reaction (hydrothermal cell, ex situ experiment) at 180 °C. This material is available free of charge via the Internet at <http://pubs.acs.org>.

#### ■ AUTHOR INFORMATION

##### Corresponding Author

\*E-mail: [rose-noelle.vannier@ensc-lille.fr](mailto:rose-noelle.vannier@ensc-lille.fr). Phone: (+33) (0) 3 20 43 65 83. Fax: (+33) (0) 33 3 20 43 68 14Tol.

##### Notes

The authors declare no competing financial interest.

#### ■ ACKNOWLEDGMENTS

The Alliance programme and ESRF, in particular, SNBL for beam time, are gratefully acknowledged. C.K. is grateful to the Royal Thai government for her Ph.D. grant funding. Nora Djelal and Laurence Burylo are acknowledged for SEM and TG-DTA analyses and conventional XRD experiments, respectively. Marielle Huvé is acknowledged for TEM. The “Fonds Européen de Développement Régional (FEDER)”, “CNRS”, “Région Nord Pas-de-Calais”, and “Ministère de l'Éducation Nationale de l'Enseignement Supérieur et de la Recherche” are acknowledged for funding of X-ray and TEM facilities.

#### ■ REFERENCES

- (1) Aurivillius, B. *Ark. Kemi* **1949**, *1*, 463.
- (2) Batist, P. A.; Kapteijns, C. J.; Lippens, B. C.; Schuit, G. C. A. *J. Catal.* **1967**, *7*, 33.
- (3) Peacock, J. M.; Parker, A. J.; Ashmore, P. G.; Hockey, J. A. *J. Catal.* **1969**, *15*, 398.
- (4) Han, Y. H.; Ueda, W.; Moro-Oka, Y. *J. Catal.* **1999**, *186*, 75.

- (5) Brazdil, J. F.; Suresh, D. D.; Grasselli, R. K. *J. Catal.* **1980**, *66*, 347.
- (6) Abraham, F.; Debreuille-Gresse, M. F.; Mairesse, G.; Nowogrocki, G. *Solid State Ionics* **1988**, *28–30*, 529.
- (7) Vannier, R. N.; Mairesse, G.; Abraham, F.; Nowogrocki, G. *J. Solid State Chem.* **1993**, *103*, 441.
- (8) Lazure, S.; Vernochet, C.; Vannier, R. N.; Nowogrocki, G.; Mairesse, G. *Solid State Ionics* **1996**, *90*, 117.
- (9) Löfberg, A.; Boujmia, S.; Capoen, E.; Steil, M. C.; Pirovano, C.; Vannier, R. N.; Mairesse, G.; Bordes-Richard, E. *Catal. Today* **2004**, *91–92*, 79.
- (10) Pirovano, C.; Lofberg, A.; Bodet, H.; Bordes-Richard, E.; Steil, M.; Vannier, R. N. *Solid State Ionics* **2006**, *177*, 2241.
- (11) Park, B. H.; Kang, B. S.; Bu, S. D.; Noh, T. W.; Lee, J.; Jo, W. *Nature* **1999**, *410*, 682.
- (12) Wolfe, R. W.; Newnham, R. E. *J. Electrochem. Soc.* **1969**, *116*, 832.
- (13) Korbzunova, L. *Ferroelectrics* **1992**, *134*, 175.
- (14) Theobald, F.; Laarif, A.; Hewat, A. W. *Ferroelectrics* **1984**, *56*, 219.
- (15) Batist, P. A.; Bouwens, J. F. H.; Schuit, G. C. A. *J. Catal.* **1972**, *25*, 1.
- (16) Thang, L. M.; Bac, L. H.; Driessche, I. V.; Hoste, S.; Van Well, W. J. M. *Catal. Today* **2008**, *131*, 566.
- (17) Wildberger, M. D.; Grunwaldt, J. D.; Maciejewski, M.; Mallat, T.; Baiker, A. *Appl. Catal., A* **1998**, *175*, 11.
- (18) Le, M. T.; Well, W. J. M. V.; Driessche, I. V.; Hoste, S. *Appl. Catal., A* **2004**, *267*, 227.
- (19) Yoshimura, M.; Somiya, S. *Mater. Chem. Phys.* **1999**, *61*, 1.
- (20) Beale, A.; Sankar, G. *Nucl. Instrum. Methods Phys. Res., Sect. B* **2003**, *199*, 504.
- (21) Li, H.; Liu, C.; Li, K. *J. Mater. Sci.* **2008**, *43*, 7026.
- (22) Beale, A. M.; Sankar, G. *Chem. Mater.* **2003**, *15*, 146.
- (23) Beale, A. M.; Reilly, L. M.; Sankar, G. *Appl. Catal., A* **2007**, *325*, 290.
- (24) Kongmark, C.; Martis, V.; Rubbens, A.; Pirovano, C.; Löfberg, A.; Sankar, G.; Vannier, R. N.; Bordes-Richard, E.; van Beek, W. *Chem. Commun.* **2009**, 4850.
- (25) Kongmark, C.; Martis, V.; Pirovano, C.; Löfberg, A.; van Beek, W.; Sankar, G.; Rubbens, A.; Cristol, S.; Vannier, R. N.; Bordes-Richard, E. *Catal. Today* **2010**, *157*, 257.
- (26) Ravel, B.; Newville, M. *J. Synchrotron Radiat.* **2005**, *12*, 537.
- (27) Newville, M. *J. Synchrotron Radiat.* **2001**, *8*, 322.
- (28) Rodriguez-Carvajal, J. *Int. Union Crystallogr., Newsletter* **2001**, *26*, 12.
- (29) Thompson, P.; Cox, D. E.; Hastings, J. B. *J. Appl. Crystallogr.* **1987**, *20*, 79.
- (30) Boccaleri, E.; Carniato, F.; Croce, G.; Viterbo, D.; van Beek, W.; Emerich, H.; Milanesio, M. *J. Appl. Crystallogr.* **2007**, *40*, 684.
- (31) Hardcastle, F.; Wachs, I. *J. Raman Spectrosc.* **1990**, *21*, 683.
- (32) Lucazeau, G.; Machon, D. *J. Raman Spectrosc.* **2006**, *37*, 189.
- (33) Scancoski, J. C.; Cavalcante, L. S.; Marana, N. L.; da Silva, R. O.; Tranquilin, R. L.; Joya, M. R.; Pizani, P. S.; Varela, J. A.; Sambrano, J. R.; Siu, L. M.; Longo, E.; Andrés, J. *Curr. Appl. Phys.* **2010**, *10*, 614.
- (34) Machon, D.; Frieze, K.; Breczewski, T.; Grzechnik, A. *J. Solid State Chem.* **2010**, *183*, 2558.
- (35) Rubbens, A.; Drache, M.; Roussel, P.; Wignacourt, J. P. *Mater. Res. Bull.* **2007**, *43*, 1683.
- (36) Gattow, G. Z. *Anorg. Allg. Chem.* **1959**, *298*, 64.
- (37) Abrahams, I.; Liu, X.; Hull, S.; Norberg, S. T.; Krok, F.; Konzanecka-Szmigiel, A.; Islam, M. S.; Stokes, S. J. *Chem. Mater.* **2010**, *22*, 4435.
- (38) Williamson, G. K.; Hall, W. H. *Acta Metall.* **1953**, *1*, 22.
- (39) Trifiro, F.; Hoster, H.; Scale, R. D. *J. Catal.* **1972**, *25*, 12.
- (40) Järvinen, M. *J. Appl. Crystallogr.* **1993**, *26*, 525.
- (41) Antonio, M.; Teller, R.; Sandstrom, D.; Mehicic, M.; Brazdil, J. *J. Phys. Chem.* **1988**, *92*, 2939.
- (42) Maczka, M.; Paraguassu, W.; Macalik, L.; Freire, P. T. C.; Hanuza, J.; Mendes Filho, J. *J. Phys.: Condens. Matter* **2011**, *23*, 045401.
- (43) Johnson, W. A.; Mehl, R. F. *Trans. Am. Inst. Min., Metall. Pet. Eng.* **1939**, *135*, 416.
- (44) (a) Avrami, M. *J. Chem. Phys.* **1939**, *7*, 1103; (b) **1940**, *8*, 212.
- (45) Avrami, M. *J. Chem. Phys.* **1941**, *9*, 177–184.
- (46) Erofe'ev, B. V. *C. R. (Dokl.) Acad. Sci. URSS* **1946**, *52*, 511.
- (47) Hancock, J. D.; Sharp, J. H. *J. Am. Ceram. Soc.* **1972**, *55*, 74.
- (48) Hulbert, S. F. *J. Br. Ceram. Soc.* **1969**, *6*, 11.
- (49) Buttrey, D. J.; Vogt, T.; Wildgruber, U.; Robinson, W. R. *J. Solid State Chem.* **1994**, *111*, 118.
- (50) Vannier, R. N.; Mairesse, G.; Abraham, F.; Nowogrocki, G. *J. Solid State Chem.* **1996**, *122*, 394.
- (51) Vannier, R. N.; Abraham, F.; Nowogrocki, G.; Mairesse, G. *J. Solid State Chem.* **1999**, *142*, 294.
- (52) Galy, J.; Hernandez-Velasco, J.; Landa-Canovas, A. R.; Vila, E.; Castro, A. *J. Solid State Chem.* **2009**, *182*, 1177.
- (53) Landa-Canovas, A. R.; Vila, E.; Hernandez-Velasco, J.; Galy, J.; Castro, A. *Acta Crystallogr., Sect. B* **2009**, *65*, 458.
- (54) Sue, J. S.; Antonio, M. R.; Soderholm, L. *Chem. Mater.* **1995**, *7*, 333.